
SUCCESS PROBABILITY IN MULTI-VIEW IMAGING

Vadim Holodovsky

Viterbi Faculty of Electrical Engineering,
Technion - Israel Institute of Technology,
Haifa, Israel
vholod@technion.ac.il

Masada Tzabari

Viterbi Faculty of Electrical Engineering,
Technion - Israel Institute of Technology,
Haifa, Israel
masada.tzemach@mail.huji.ac.il

Yoav Schechner

Viterbi Faculty of Electrical Engineering,
Technion - Israel Institute of Technology,
Haifa, Israel
yoav@ee.technion.ac.il

Alex Frid

Norman & Helen Asher Space Research Institute,
Technion - Israel Institute of Technology,
Haifa, Israel
alex.frid@gmail.com

Klaus Schilling

Zentrum für Telematik e.V.,
Würzburg, Germany
klaus.schilling@telematik-zentrum.de

August 1, 2024

ABSTRACT

Platforms such as robots, security cameras, drones and satellites are used in multi-view imaging for three-dimensional (3D) recovery by stereoscopy or tomography. Each camera in the setup has a field of view (FOV). Multi-view analysis requires overlap of the FOVs of all cameras, or a significant subset of them. However, the success of such methods is not guaranteed, because the FOVs may not sufficiently overlap. The reason is that pointing of a camera from a mount or platform has some randomness (noise), due to imprecise platform control, typical to mechanical systems, and particularly moving systems such as satellites. So, success is probabilistic. This paper creates a framework to analyze this aspect. This is critical for setting limitations on the capabilities of imaging systems, such as resolution (pixel footprint), FOV, the size of domains that can be captured, and efficiency. The framework uses the fact that imprecise pointing can be mitigated by self-calibration - provided that there is sufficient overlap between pairs of views and sufficient visual similarity of views. We show an example considering the design of a formation of nanosatellites that seek 3D reconstruction of clouds.

Keywords Multi-view Imaging · Geometric self-calibration

1 Introduction

Multi-viewing imaging systems are common (Fig. 1) and include: Rigs of security or other monitoring cameras observing a volumetric domain; Cooperating drones observing the same scene, which may be volumetric or a surface domain; or a fleet of satellites in a formation observing a thin atmospheric domain just above the Earth's surface. Multi-view setups also include a moving platform observing sequentially any such domain. Multi-view setups enable three-dimensional (3D) surface reconstruction and computed tomography (CT) outdoors, including CT of turbulence [1, 2] or clouds [3, 4, 5, 6], and statistical tomography of microscopic organisms [7]. Deep-neural networks (DNNs) currently advance large-scale CT [8, 9, 10, 5]. DNNs also advance surface recovery based on multi-view stereo [11, 12, 13, 14, 15, 16].

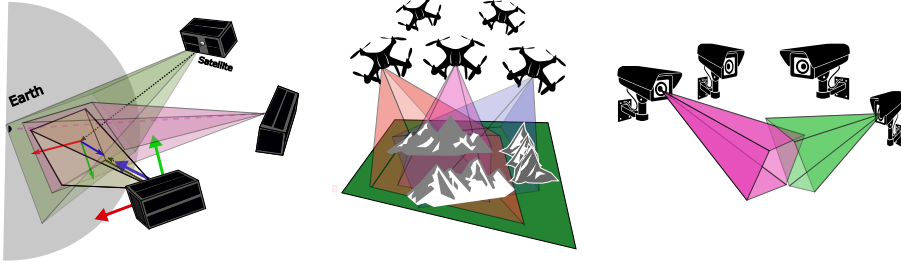


Figure 1: Pointing errors across multi-view platforms: [Left] Satellites having alignment challenges during Earth observation. [Middle] Drones having orientation noise. [Right] The same phenomenon can be seen in ground-based (e.g, security) cameras.

As cameras and agile platforms become very affordable (not least by cameras being in smartphones), such uses are set to broaden, particularly using compact, low-resource platforms. However, the success of 3D recovery relies, first of all, on having the right data, that is, having the domain of interest in overlapping views from a sufficient number of viewpoints. This is not guaranteed. Ideally, a platform carrying a camera would point in a direction it is commanded to, with perfect accuracy. But platforms used to position and orient cameras invariably introduce pose knowledge errors. Each platform has limited accuracy in pointing and pose sensing. Consequently, there is a random error between the actual pointing direction and a commanded direction [17] given to the platform aiming system. The standard deviation of this error is termed *absolute pointing error* (APE). This problem is exacerbated in small, low-resource platforms. The cause is mechanical inaccuracies and feedback, especially in moving platforms such as small satellites and drones, which rely on an attitude determination and control system (ADCS) [17]. Therefore, the success of multi-view imaging is probabilistic.

This paper creates a framework to analyze the success probability. This is critical for setting limitations on the capabilities of imaging systems, such as resolution (pixel footprint), FOV, the size of domains that can be captured, and efficiency. To the best of our knowledge, this kind of analysis has not been done before.

The framework relates to self-calibration. Geometric self-calibration is thoroughly developed in computer vision [18, 19, 20]. It can help detect pose errors, e.g, using structure from motion [19, 21, 22, 23] *after image data had already been acquired* [24, 20, 19, 25, 26]. However, extrinsic geometric self-calibration requires the following:

- (a) A sufficient overlap of the fields of view (FOVs), specifically between FOVs corresponding to nearest-neighboring viewpoints.
- (b) A sufficient number of geometric features in the region of the overlapping FOVs. Each camera should view identifiable features, that can be identified from at least one other view.

The framework of this paper relies on these principles. Together with a noise model of pointing, we derive the probability for self-calibration to succeed, and consequently, for 3D reconstruction to succeed.

As a case study, we apply this analysis to considerations that should be addressed by designers of space missions. Due to their relatively low production and launch costs, there is a growing trend towards deploying formations of small satellites for Earth observation missions [27, 28, 29, 30, 31, 32]. However, they often trade-off affordability and scalability for limited pointing capabilities, when compared to large satellites [33, 34, 35, 36, 37, 38]. This presents unique challenges for 3D imaging tasks, where precise alignment and overlap of images from multiple spaceborne views are crucial for accurate data analysis.

2 Overlap Measures

Fig. 2 illustrates the concept of overlap between FOVs on a reference surface. Let c denote an index of a camera. Assume identical cameras within the setup. Each camera has a frustum of vision: a pyramid-shaped volume that starts at the camera optical center and extends in 3D, as in Fig. 2 and [39]. The intersection of the frustum of camera c with a reference surface creates a polygonal $\text{FOV}[c]$, which we describe in section 4. Let N_{cam} be the number of cameras in a multi-view setup. The setup yields a set of polygons $\Psi = \{\text{FOV}[c]\}_{c=1}^{N_{\text{cam}}}$. Set one camera as an *anchor*. Often, users are most interested in observing the finest details of an object of interest. Therefore, the anchor is the camera closest to the domain of interest. Consequently, $|\text{FOV}[\text{anchor}]| \leq |\text{FOV}[c]|, \forall c$. Overlap-related terms are defined as follows:

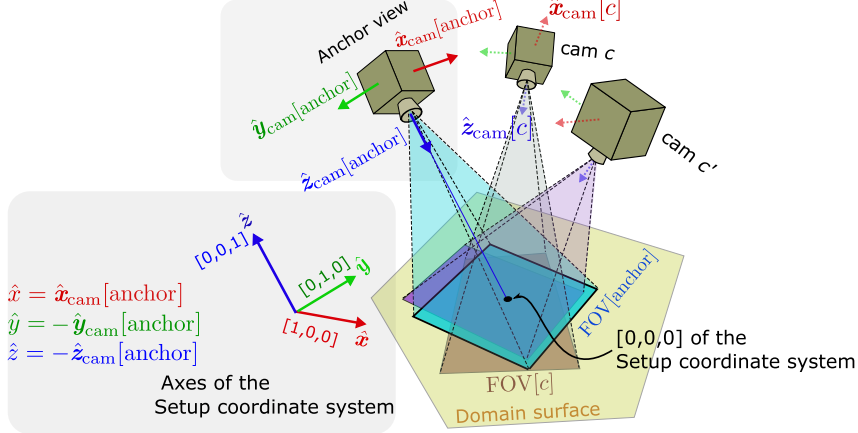


Figure 2: A general multi-view setup. One of the cameras is the anchor. Its axes and location correspond to the setup coordinate system. Each camera has a FOV on the domain surface.

- *Absolute-Overlap* is the total area of overlap of FOVs of N_{cam} views:

$$\text{AO} = \left| \bigcap_{c=1}^{N_{\text{cam}}} \text{FOV}[c] \right|. \quad (1)$$

- *Relative-Overlap* of N_{cam} views:

$$\text{RO} = \frac{\text{AO}}{|\text{FOV}[{\text{anchor}}]|} \leq 1. \quad (2)$$

- *Relative pair-wise overlap* of views c and c' is

$$\text{RO}_{c,c'} = \frac{|\text{FOV}[c] \cap \text{FOV}[c']|}{\min\{|\text{FOV}[c]|, |\text{FOV}[c']|\}} \leq 1. \quad (3)$$

- *Mean Absolute-Overlap* $\overline{\text{AO}} = \langle \text{AO} \rangle$, is the average of AO, resulting from N_{MC} random samples of Ψ . In section 5, we detail how to obtain statistics of these terms by using Monte Carlo sampling.
- *Mean Relative-Overlap* $\overline{\text{RO}} = \langle \text{RO} \rangle$, is the RO averaged over N_{MC} random samples of Ψ , each generated by Monte-Carlo.

section 1 lists conditions for successful self-calibration of geometric parameters. Here, we elaborate on how to measure the probability of meeting issue (a). A key term is *connected* view pairs. Let $\mu_{c,c'}$ be the angular difference between cameras indexed c and c' . The visual similarity between views c and c' depends on $\mu_{c,c'}$. For successful geometric self-calibration of an image pair, we need a sufficient number of visually similar image features. Therefore, it is important that the following coexists:

- A small $\mu_{c,c'}$, in order to have sufficient similarity. This means that visual features are similar between views c and c' .
- A large $\text{RO}_{c,c'}$, in order to have a sufficient number of matching visual features within the domain.

If $\mu_{c,c'}$ is large, images c and c' may significantly differ, resulting in very few or null matching feature points between the views. We assume that for a threshold μ_{max} , if $\mu_{c,c'} \leq \mu_{\text{max}}$, then features are likely to be matched.

Let $T \in [0, 1]$ be a unitless threshold; representing the minimally required RO of any pair of views c and c' . In other words, we need $\text{RO}_{c,c'} \geq T$ for successful pair-wise self-calibration. We distinguish between the above critical conditions. The similarity issue depends on the *scene*, not the setup. For example, colorful bright particles that shine isotropically are visually identified even from mutually very distant views. In contrast, features on complex 3D shapes such as trees and turbulent clouds are hard to identify and match visually, even from angularly close views. The aspect $\text{RO}_{c,c'} \geq T$ is a property of the setup. This issue can be engineered by the optics.

2.1 Connected graph

Let Q be the number of viewpoints to undergo geometric self-calibration. To achieve geometric self-calibration for each of the Q views, any view must have a significant FOV overlap with some other view, i.e., the setup must have pair-wise overlaps. Here we relate connected pair-wise overlaps to a *connected graph* concept. Let $B(Q)$ denote a *connected* set of Q views within the setup, i.e., $B(Q)$ is a cluster of Q views. Fig. 3 shows the concept of $B(Q)$ as a connected set represented by a graph. Graph edges between two views (graph nodes) c and c' express that the requirements on the two critical conditions above are met. Fig. 3[Right], shows a connected graph having $B(Q = 5)$. There, pair-wise self-calibration propagates across all views. Fig. 3[Left] shows a graph of two disconnected components. In the $B(Q = 3)$ cluster, geometric self-calibration can use three views of the setup. The other two views cannot be self-calibrated with the $B(Q = 3)$ cluster.

Define $P_{\text{calib}}(T \mid |\text{FOV}[\text{anchor}]|, \text{APE}, Q)$ as the probability that a set of *at least* Q views can be self-calibrated. To estimate $P_{\text{calib}}(T \mid |\text{FOV}[\text{anchor}]|, \text{APE}, Q)$, we use Monte-Carlo, as we describe in section 6. Let $N_{B(Q)}$ be the number of Monte Carlo samples, in which any Q views create a cluster $B(Q)$. Fig. 4 shows an example using $N_{\text{MC}} = 5$. Here, there is one sample with $B(3)$, one sample with $B(5)$, two samples with $B(3)$, and two samples with $B(4)$. The probability to have component of $B(5)$ is $\frac{B(Q)}{N_{\text{MC}}} = 1/5$, and component of $B(4)$ is $2/5$. The probability of getting a cluster with *at least* three nodes is $B(3) + B(4) + B(5) = 1$. To generalize, the probability to have a $B(Q)$ component is $N_{B(Q)}/N_{\text{MC}}$. Therefore,

$$P_{\text{calib}}(T \mid |\text{FOV}[\text{anchor}]|, \text{APE}, Q) \approx \sum_{Q'=Q}^{N_{\text{cam}}} \frac{N_{B(Q')}}{N_{\text{MC}}}. \quad (4)$$

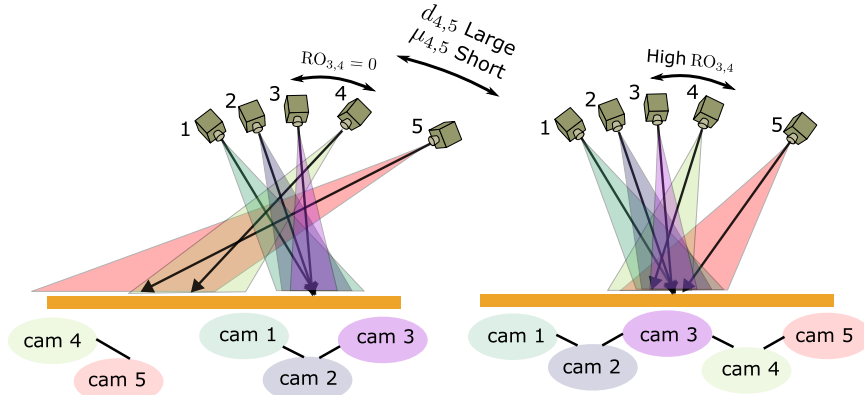


Figure 3: [Left] Disconnected views (nodes). In this example, there are two graph components, $B(Q = 3)$ and $B(Q = 2)$. [Right] A graph of a connected set of views. Connection is marked by an edge. An edge between nodes c and c' means that $\text{RO}_{c,c'} > T$ and $\mu_{c,c'} \leq \mu_{\text{max}}$. The graph has a single component $B(Q = 5)$.

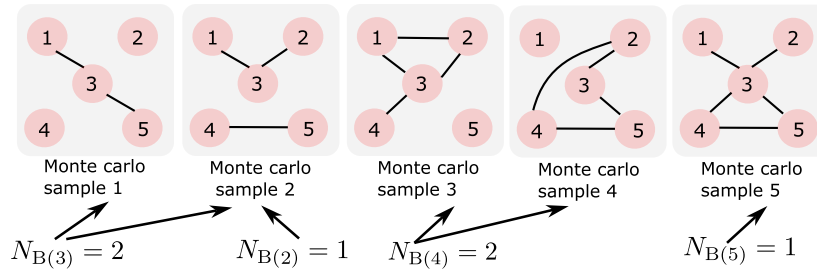


Figure 4: Example of estimation of components of P_{calib} via Monte Carlo with $N_{\text{MC}} = 5$.

Any Monte Carlo sample creates a random state Ψ . Using N_{MC} samples, we can estimate P_{calib} . Eq. (4) expresses the probability of achieving geometric self-calibration using Q views.

3 Pointing noise

3.1 Coordinate systems

Two coordinate systems (Fig. 2) are referred to throughout the paper.

1. The *setup coordinate system* has an origin on the domain surface, typically the ground. It is right-handed. The axes are labeled \hat{x} , \hat{y} , and \hat{z} .
2. The *camera coordinate system* is right-handed. Per camera c , the axes of the camera coordinate system are denoted $\hat{x}_{\text{cam}}[c]$, $\hat{y}_{\text{cam}}[c]$, $\hat{z}_{\text{cam}}[c]$. Axis $\hat{z}_{\text{cam}}[c]$ aligns with the optical axis of the camera c . Axes $\hat{x}_{\text{cam}}[c]$ and $\hat{y}_{\text{cam}}[c]$ are parallel to the pixel rows and columns of the sensor of camera c , respectively [40].

The anchor camera relates these two coordinate systems. In our context, the origin of the setup coordinate system is the intersection of a line of sight from the anchor camera (in the direction of $\hat{z}_{\text{cam}}[\text{anchor}]$) with the reference surface (Fig. 2). Therefore, $\hat{z} = -\hat{z}_{\text{cam}}[\text{anchor}]$, $\hat{x} = \hat{x}_{\text{cam}}[\text{anchor}]$, and $\hat{y} = -\hat{y}_{\text{cam}}[\text{anchor}]$.

Let $\mathbf{R}[c]$ denote a camera c rotation matrix from the camera coordinate system to the setup coordinate system. Let us denote a general vector in the setup coordinate system by \mathbf{v} and a general vector in the camera coordinate system of camera c by $\mathbf{v}^{\text{cam}}[c]$, then

$$\mathbf{v} = \mathbf{R}[c] \mathbf{v}^{\text{cam}}[c]. \quad (5)$$

3.2 Ideal pointing

Let $\mathbf{u}_{\text{cam}}[c] = [X_{\text{cam}}[c], Y_{\text{cam}}[c], Z_{\text{cam}}[c]]^\top$ denote the location of camera c in the setup coordinate system, where $(\cdot)^\top$ denotes transposition. Suppose all cameras rotate to point to the origin of the setup coordinate system [0,0,0][km] (Fig. 2). To achieve this, define matrix $\mathbf{R}[c]$ using the *LookAt transform* [41], as follows. First, set all the cameras such that the 3D vector along the sensor pixel columns is $\hat{y}_{\text{cam}}[c] = [0, -1, 0]^\top$, $\forall c$. Then, point the camera optical axis $\hat{z}_{\text{cam}}[c]$ towards the target (look at position). Afterwards, rotate the transform using the up direction to of the camera, which is $\hat{y}_{\text{cam}}[c]$. Note that $\hat{y}_{\text{cam}}[c]$ is updated, to match a right-hand coordinate system.

$$\mathbf{R}[c] = \left[\hat{y}_{\text{cam}}[c] \times \frac{-\mathbf{u}_{\text{cam}}[c]}{\|\mathbf{u}_{\text{cam}}[c]\|}, \quad \frac{-\mathbf{u}_{\text{cam}}[c]}{\|\mathbf{u}_{\text{cam}}[c]\|} \times \hat{y}_{\text{cam}}[c] \times \frac{-\mathbf{u}_{\text{cam}}[c]}{\|\mathbf{u}_{\text{cam}}[c]\|}, \quad \frac{-\mathbf{u}_{\text{cam}}[c]}{\|\mathbf{u}_{\text{cam}}[c]\|} \right]. \quad (6)$$

3.3 Pointing noise

Due to pointing errors of the platform carrying the camera, the orientation of each camera may deviate from that desired. Let $\bar{\mathbf{R}}[c]$ be a noisy rotation matrix of camera c relative to the setup coordinate system. Let $\bar{\mathbf{v}}$ be a noisy version of the vector \mathbf{v} . Using Eq. (5),

$$\bar{\mathbf{v}} = \bar{\mathbf{R}}[c] \mathbf{v}^{\text{cam}}[c]. \quad (7)$$

From eq. (5), $\mathbf{v}^{\text{cam}}[c] = \mathbf{R}[c]^\top \mathbf{v}$. So,

$$\bar{\mathbf{v}} = \bar{\mathbf{R}}[c] \mathbf{R}[c]^\top \mathbf{v} = \delta\mathbf{R}[c] \mathbf{v}, \quad (8)$$

where

$$\delta\mathbf{R}[c] = \bar{\mathbf{R}}[c] \mathbf{R}[c]^\top, \quad \bar{\mathbf{R}}[c] = \delta\mathbf{R}[c] \mathbf{R}[c]. \quad (9)$$

The matrix $\delta\mathbf{R}[c]$ transforms $[\hat{x}_{\text{cam}}[c], \hat{y}_{\text{cam}}[c], \hat{z}_{\text{cam}}[c]]$ to noisy axes of the camera $[\hat{x}'_{\text{cam}}[c], \hat{y}'_{\text{cam}}[c], \hat{z}'_{\text{cam}}[c]]$ (Fig. 5[Left]).

To simulate pointing noise, we sample $\delta\mathbf{R}[c]$ as follows: First, we sample a vector $\boldsymbol{\omega} = [\omega_x, \omega_y, \omega_z]^\top$ from a uniform distribution on a unit sphere.¹ Then, we sample an angle Θ from a Gaussian distribution around $\boldsymbol{\omega}$. The standard deviation of the angle Θ [degrees] is the APE. Therefore, $\Theta \sim \mathcal{N}(0, \text{APE})$.

Let $C = \cos\Theta$ and $S = \sin\Theta$. The rotation matrix $\delta\mathbf{R}[c]$ is a function of Θ and $\boldsymbol{\omega}$, and it is calculated by Rodrigues' formula [42, 39],

$$\delta\mathbf{R}(\Theta, \boldsymbol{\omega})[c] = \begin{bmatrix} C + \omega_x^2(1 - C), & \omega_x\omega_y(1 - C) - \omega_zS, & \omega_x\omega_z(1 - C) + \omega_yS \\ \omega_x\omega_y(1 - C) + \omega_zS, & C + \omega_y^2(1 - C), & \omega_y\omega_z(1 - C) - \omega_xS \\ \omega_x\omega_z(1 - C) + \omega_yS, & \omega_z\omega_y(1 - C) + \omega_xS, & C + \omega_z^2(1 - C) \end{bmatrix}. \quad (10)$$

¹If the pointing error model has a preferred orientation of $\boldsymbol{\omega}$, an anisotropic approach should be used: $\boldsymbol{\omega}$ is to be sampled from an anisotropic distribution.

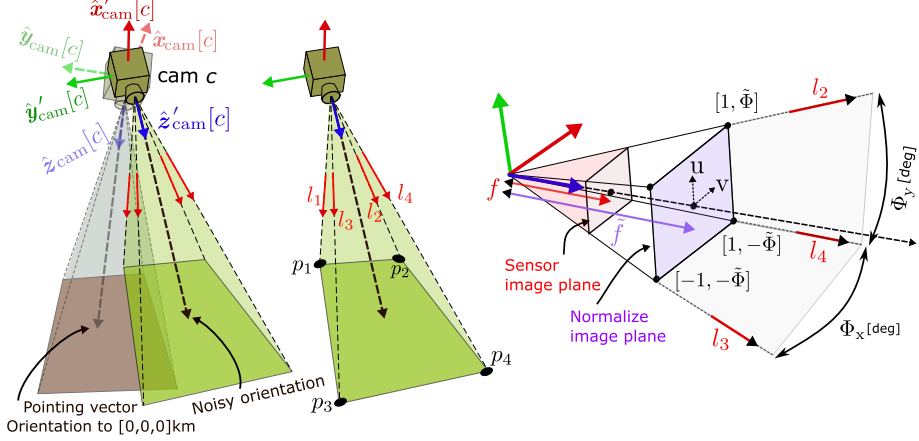


Figure 5: [Left] The camera coordinate system and the effect of noisy pointing. [Middle] Four rays bound the FOV frustum in 3D. [Right] The camera FOV frustum, image sensor plane, normalized image plane and angular FOV parameters.

To recap, noisy pointing is simulated as follows. First, we calculate the camera axes vectors in the setup coordinate system $[\hat{x}_{\text{cam}}[c], \hat{y}_{\text{cam}}[c], \hat{z}_{\text{cam}}[c]]$ at ideal pointing, using Eq. (6). Then, Eqs. (9,10) create random rotations $\delta\mathbf{R}[c]$, $\mathbf{R}[c]$. This yields perturbed camera axes vectors relative to the setup coordinate system,

$$\hat{z}'_{\text{cam}}[c] = \bar{\mathbf{R}}[c] [0, 0, 1]^\top, \quad \hat{y}'_{\text{cam}}[c] = \bar{\mathbf{R}}[c] [0, 1, 0]^\top, \quad \hat{x}'_{\text{cam}}[c] = \bar{\mathbf{R}}[c] [1, 0, 0]^\top. \quad (11)$$

4 Field of view

Sec. 2 introduced the frustum of a camera FOV. This volume intersects with the domain surface, creating a 2D FOV. This section follows these calculations.² Let $\Phi = [\Phi_x, \Phi_y] \text{[deg]}$ denote the angular FOV of a camera in its internal row and column dimensions, and let $[\Phi_y/\Phi_x] \equiv \tilde{\Phi} \leq 1$. Define a *normalized image plane* (Fig. 5[Right]), corresponding to a unit-less focal length

$$\tilde{f} = [\tan(\Phi_x/2)]^{-1}. \quad (12)$$

In the normalized image plane, pixel coordinates are $u \in [-1, 1]$ and $v \in [-\tilde{\Phi}, \tilde{\Phi}]$ as shown in Fig. 5[Right]. The intrinsic matrix [39] of the normalized camera is

$$\mathbf{K} = \begin{bmatrix} \tilde{f} & 0 & 0 \\ 0 & \tilde{f} & 0 \\ 0 & 0 & 1 \end{bmatrix}. \quad (13)$$

A pixel at $[u, v]$ in normalized camera c that is rotated by noisy rotation $\bar{\mathbf{R}}[c]$, relates to a vector $\mathbf{l}[c]$ in the 3D setup coordinate system is

$$\mathbf{l}[c] = \bar{\mathbf{R}}[c] \mathbf{K}^{-1} [u, v, 1]^\top. \quad (14)$$

The rays that bound the frustum FOV (Fig. 5[Middle]) have direction vectors $\{\mathbf{l}_1[c], \mathbf{l}_2[c], \mathbf{l}_3[c], \mathbf{l}_4[c]\}$ that can be calculated using Eq. (14),

$$\begin{aligned} \mathbf{l}_1[c] &= \bar{\mathbf{R}}[c] \mathbf{K}^{-1} [-1, \tilde{\Phi}, 1]^\top, & \mathbf{l}_2[c] &= \bar{\mathbf{R}}[c] \mathbf{K}^{-1} [1, \tilde{\Phi}, 1]^\top, \\ \mathbf{l}_3[c] &= \bar{\mathbf{R}}[c] \mathbf{K}^{-1} [-1, -\tilde{\Phi}, 1]^\top, & \mathbf{l}_4[c] &= \bar{\mathbf{R}}[c] \mathbf{K}^{-1} [1, -\tilde{\Phi}, 1]^\top. \end{aligned} \quad (15)$$

Along a ray, a point is parameterized by t using,

$$\begin{aligned} \mathbf{l}_1[c] &= \mathbf{u}_{\text{cam}}[c] + \mathbf{l}_1[c]t, & \mathbf{l}_2[c] &= \mathbf{u}_{\text{cam}}[c] + \mathbf{l}_2[c]t, \\ \mathbf{l}_3[c] &= \mathbf{u}_{\text{cam}}[c] + \mathbf{l}_3[c]t, & \mathbf{l}_4[c] &= \mathbf{u}_{\text{cam}}[c] + \mathbf{l}_4[c]t. \end{aligned} \quad (16)$$

For each ray in eq. (16), we calculate the intersection with the domain surface. The result is four points on the domain surface, which defines the surface $\text{FOV}[c]$. If the surface is flat, then $\text{FOV}[c]$ is a polygon, whose vectors in fig. 5[Middle] are $\{[p_1, p_2, p_3, p_4]\}$.

²A commonly done, the camera model here is perspective. Intrinsic calibration can correct for distortions.

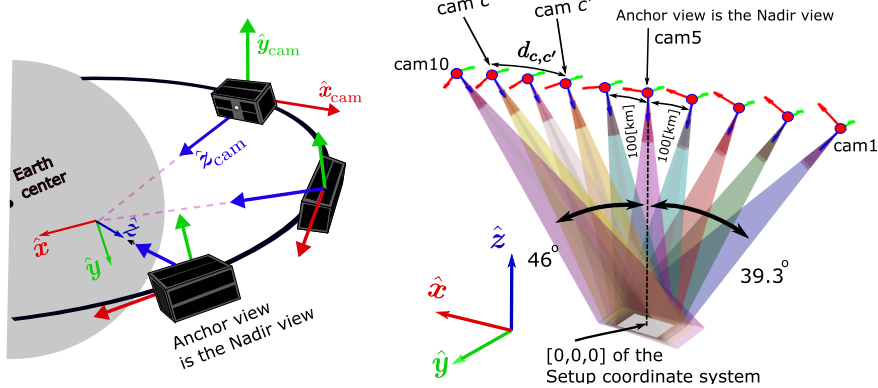


Figure 6: A string of pearls satellite formation setup observing the same domain. [Left] The setup as it is seen from space. [Right] The setup is aligned with the orbital plane.

5 Satellites in a formation

As a case study, consider simultaneous multi-view imaging of clouds by a formation of small satellites as planned in the CloudCT and C3IEL missions [43, 27, 40, 44]. Multi-view imaging doesn't necessarily need to have a simultaneous setup. Some satellites use sequential acquisition to achieve multi-view. For instance, the Multiangle Imaging SpectroRadiometer [45] used to measure 3D of clouds, tomography of clouds, and aerosol optical depth. The Mesospheric Airglow/Aerosol Tomography and Spectroscopy [46, 47], the airborne Gimballed Limb Observer for Radiance Imaging of the Atmosphere [48, 49] for tomography of mesoscale gravity waves. The Microwave Limb Sounder [50, 51] to measures the composition and temperature of the lower atmosphere layers.

The CloudCT setup provides a framework for passive multi-view tomography of the domain. For tomography, multiple satellites should have overlapping FOV near Earths' surface. To enable multiple satellites in an affordable budget, each satellite should be small. Small satellites have limited resources, and usually carry coarser sensors than large satellites. Therefore, nanosatellites have a high APE.

Fig. 6 illustrates a *string of pearls* formation: The satellites move consecutively in the same orbit. Each satellite carries a camera and tries points to the same region as the anchor camera. The anchor, i.e. the camera closest to the domain, is nadir-viewing. The domain zenith is \hat{z} (Fig. 7). The angle between this zenith and spaceborne camera c is $\xi_{cam}[c]$, relative to the center of the Earth. Then, $\xi_{cam}[\text{anchor}] = 0$.

Earth is approximately a sphere having radius H_{earth} [km]. The altitude of the orbit is H_{orbit} [km]. The orbit radius from the Earth's center is $H = H_{\text{earth}} + H_{\text{orbit}}$. The 3D location of a camera in the setup coordinate system is

$$X_{cam}[c] = H \sin(\xi_{cam}[c]), \quad Y_{cam}[c] = 0, \quad Z_{cam}[c] = H \cos(\xi_{cam}[c]) - H_{\text{earth}}. \quad (17)$$

The distance between nearest-neighboring satellites on the orbit arc is denoted by L [km] and it is uniform over the setup. Let $\Delta\xi_{cam} = \frac{L}{H}$. According to the example in Figs. 6, 7, the rightmost satellite has index $c = 1$. For an even N_{cam} ,

$$\xi_{cam}[c] = (c - N_{\text{cam}}/2)\Delta\xi_{cam}. \quad (18)$$

Using Eqs. (6,11), we calculate noisy orientation of each camera c in the setup coordinate system. As long as the ground FOV is on a scale of 100×100 [km]², it is valid to neglect the curvature of the Earth, i.e., assume a regionally flat earth. The FOV on the ground is then approximately polygonal, as described in section 4. To calculate the overlap terms that intersect the FOV polygons Ψ (eq. (1)) on the flat ground surface, we used [52]. Since the anchor has nadir-view, its FOV on the domain surface is a rectangle of dimensions $\text{FOV}[\text{anchor}] = W_x \times W_y$, where

$$W_x = 2H_{\text{orbit}} \tan\left(\frac{\Phi_x}{2}\right) [\text{km}], \quad W_y = 2H_{\text{orbit}} \tan\left(\frac{\Phi_y}{2}\right) [\text{km}]. \quad (19)$$

section 2 describes criteria for successful geometric self-calibration of $Q \leq N_{\text{cam}}$ views. We use the Monte Carlo approach to estimate the probability of meeting these criteria. A *rotation state sample* is a set of random rotations across the formation, $\Omega = \{\bar{\mathbf{R}}[c]\}_{c=1}^{N_{\text{cam}}}$. The state Ω is sampled by Monte Carlo. The sampled rotation state corresponds to a set of ground FOV polygons $\Psi = \{\text{FOV}[c]\}_{c=1}^{N_{\text{cam}}}$. Then, overlap measures are calculated for this sample. Finally, we use an ensemble of such samples to obtain statistics, i.e., to estimate the probability of successful geometric self-calibration.

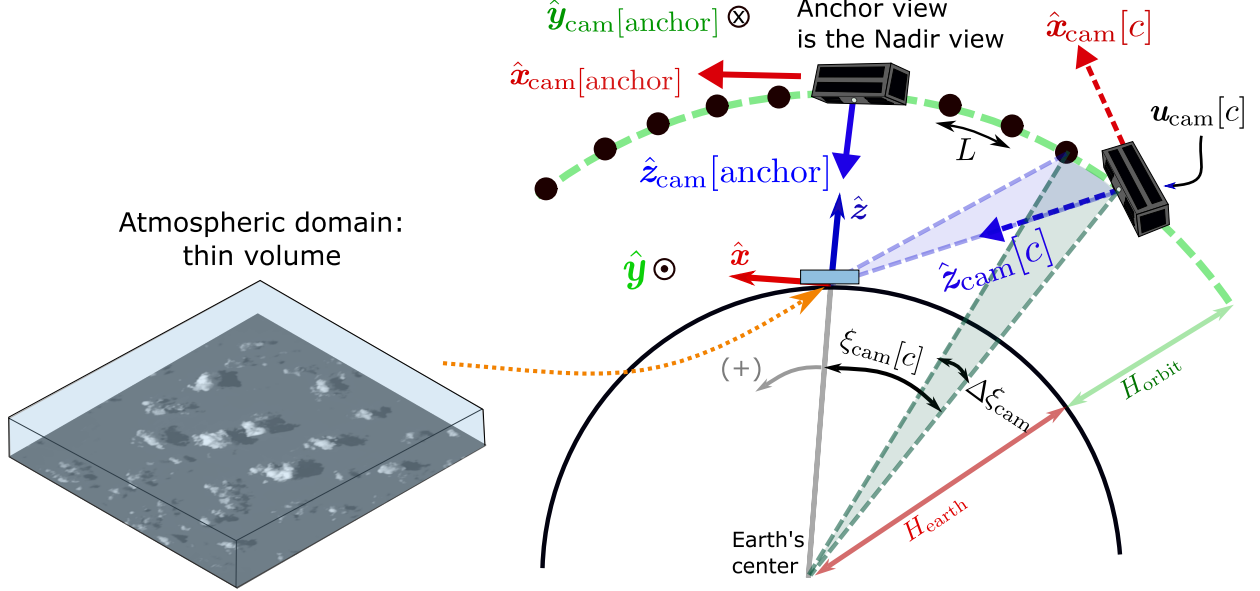


Figure 7: The setup and camera coordinate systems are shown in a simplified (two-dimensional) geometry. The observed domain is thin atmospheric volume. The origin of the domain is on the ground surface.

5.0.1 Setup considerations

As described in section 2, visual similarity between views c and c' depends on $\mu_{c,c'}$. Here, we chose to work with a distance between the satellites indexed c and c' , which we denote $d_{c,c'}$ (Fig. 6). The constraint on $d_{c,c'}$ is similar to the constraint on $\mu_{c,c'}$. If $d_{c,c'}$ is large, the images from c and c' may significantly differ, resulting in very few or null matching feature points between the views. Let us consider satellites orbiting at $H_{\text{orbit}}=500\text{-}600\text{ [km]}$, observing convective cloud fields. Then, as we explain, for sufficient similarity of clouds appearance section 2 $d_{c,c'} \leq 200\text{[km]}$.

Here is evidence for this limit. Dandini et al. [44] showed that at $H_{\text{orbit}} = 600\text{[km]}$ sufficient cloud matches require $L = 150\text{[km]}$ for which $\mu = 7^\circ$.

Zeis et al. [45] use Multiangle Imaging SpectroRadiometer (MISR) data for cloud geometry. The angle between adjacent views in Multiangle Imaging SpectroRadiometer is in the $10^\circ\text{-}26^\circ$ range (relative to the local vertical [53] as shown in Fig. 6).

In The CloudCT setup (Fig. 6), $L = 100\text{[km]}$, for a 200[km] baseline, the range of angles³ $\mu = 14^\circ\text{-}23^\circ$.

A high angular span of views is essential for a good tomography. Ref [54] reports the retrieval quality is poor at total angular spans below 60° [deg]. If the formation orbit is approximately 500 [km] , and there are 10 satellites, a high angular span of views, e.g., of 85° [deg], is possible if the distance (on the orbit arc) between nearest-neighbor satellites is around 100 [km] .

6 Results

In this section, we follow the CloudCT mission parameters and analyze the probability of successful geometric self-calibration. Based on [40], we set $H_{\text{orbit}} = 500\text{ [km]}$, $L=100\text{ [km]}$, and $N_{\text{cam}} = 10$. Most of the results here assume $W_x=100\text{ [km]}$, $W_y=70\text{ [km]}$ [55].

We set $T = 0.8$. For each analyzed case (e.g., different APE, FOV), we sample $N_{\text{MC}} = 100$ noisy rotation states. fig. 8 shows how the $\overline{\text{RO}}$ changes as a function of APE. fig. 9[a] shows the estimated $\overline{\text{RO}}$ for all 10 viewpoints, and P_{calib} . Both depend on the APE. The most significant result is of P_{calib} ; if the APE of satellites is $\approx 2^\circ$ (as typical for nanosatellites) then less than 10% of all scenes can achieve self-calibration, and consequently tomography, based on all 10 viewpoints. This seems very inefficient. However it is not necessary to use 10 views; also a smaller number of views

³The angle between views c and c' is $|\cos^{-1}(\hat{z}_{\text{cam}}[c] \cdot \hat{z}_{\text{cam}}[c'])|$. The angle between views cam6 and cam4 is $\approx 23^\circ$. The angle between views cam10 and cam8 is $\approx 14^\circ$.

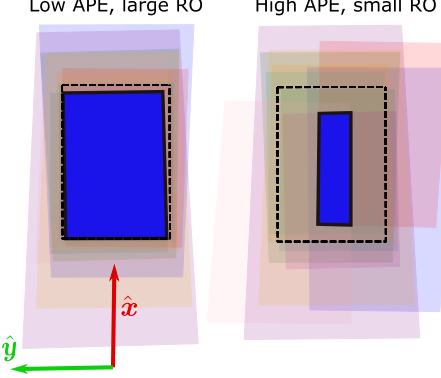


Figure 8: Footprints of ten satellites on the ground. Different colors correspond to views by different satellites. The overlap between the views is marked in blue. [Left] Small APE, and large \overline{RO} . [Right] High APE, and small \overline{RO} . The black dashed rectangle represents the footprint of the anchor view.

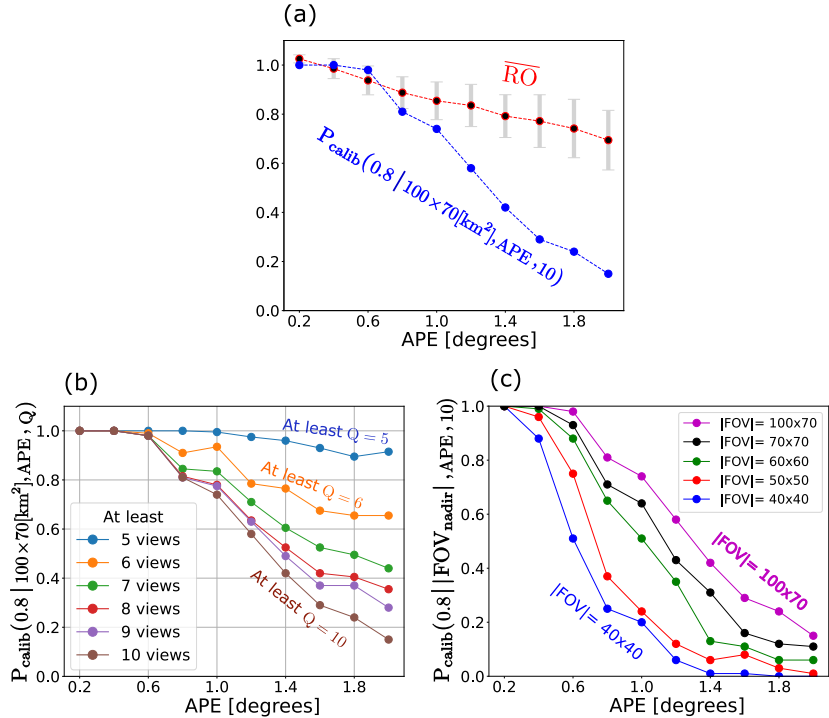


Figure 9: [a] The blue plot shows the P_{calib} with $T = 0.8$ and $Q = 10$, and the red plot shows \overline{RO} . The gray bars represent the standard deviation of the RO. [b] The P_{calib} ($T = 0.8$) as a function of $5 \leq Q \leq 10$. Different curves represent different Q . [a-b] Corresponds to $|\text{FOV}[\text{anchor}]| = 100 \times 70 \text{ km}^2$. [c] The P_{calib} ($T = 0.8$, $Q = 10$) as a function of the APE and $|\text{FOV}[\text{anchor}]|$. Different curves represent different $|\text{FOV}[\text{anchor}]|$.

can enable good science. So what happens if successful analysis can be achieved if *at least* 7 out of the 10 viewpoints can achieve self-calibration? for such a question see fig. 9[b].

It shows that P_{calib} increases when Q decreases, i.e., it is more likely to perform geometric self-calibration if we tolerate using a subset having fewer overlapping views in the setup. For $Q=7$, $\approx 50\%$ of scenes will be successfully acquired, self-calibrated and reach tomography, though with varying accuracy.

Suppose we want a better resolution, i.e., a smaller pixel footprint on Earth. Then, for a fixed sensor-array, this can only be achieved using optics that narrows the FOV. Can this be tolerated? Suppose we use a FOV of 40×40 [km], see Fig. fig. 9[c]. As seen, if the APE is greater than 1.5° , there is very low chance of success.

7 Discussion

The paper provides a framework to analyze the probability of successful geometric self-calibration, and consequently multi-view imaging of a domain, when cameras pointing is noisy. The analysis is based on a graph representation. In the graph, each node is a viewpoint. Two nodes are connected if they satisfy two conditions: (a) a large enough relative overlap between the FOVs they observe in the object domain, through a threshold T and (b) a small difference of feature appearance through a small difference in viewpoint location or direction. This is done by setting a maximum allowable viewing direction μ_{\max} , which depends of statistics of the scene: in rather flat objects having negligible occlusions, μ_{\max} can be large, but in highly complex 3D structures, such as clouds and trees, μ_{\max} should be small. The paper focused on (a), randomizing the overlap. However, future work can extend this, and randomize scenes whose statistics have varying levels of complexity.

We apply this analysis to design considerations of a satellite formation. This implications on the efficiency of the formation, i.e, how many scenes is can successfully capture, relative to the overall number it *tries* to capture. This affects the communication downlink needs. It also affects the achievable resolution: if a wider FOV is needed for a high probability of success, then a fixed sensor pixel array can only support coarser pixel footprint on the ground.

The paper focused on scenarios where pointing has significant uncertainty, but the location of cameras is well known. This is consistent with the common ability to nail down the location of each camera. This ability exists when cameras are mounted on static positions (building, posts) or when using navigation tools as GPS. However, the framework can easily extend to general pose errors due to both pointing and location. Moreover, pointing noise need not be isotropic: a perturbation axis may be more or less uncertain than others, and this can be expressed in nonuniform Monte Carlo sampling.

Acknowledgments

We thank Ilham Mammadov and Maximilian von Arnim for their advices. Yoav Schechner is the Mark and Diane Seiden Chair in Science at the Technion. He is a Landau Fellow supported by the Taub Foundation. His work was conducted in the Ollendorff Minerva Center. Minvera is funded through the BMBF. This project has received funding from the European Research Council (ERC) under the European Union’s Horizon 2020 research and innovation programme (CloudCT, grant agreement No. 810370), and the Israel Science Foundation (ISF grant 2514/23).

References

- [1] Marina Alterman, Yoav Y Schechner, Minh Vo, and Srinivasa G Narasimhan. Passive tomography of turbulence strength. In *European Conference on Computer Vision*, pages 47–60. Springer, 2014.
- [2] Nir Shaul and Yoav Y Schechner. Tomography of turbulence strength based on scintillation imaging. In *European Conference on Computer Vision*, pages 470–486. Springer, 2022.
- [3] Aviad Levis, Yoav Y. Schechner, and Anthony B. Davis. Multiple-scattering microphysics tomography. In *CVPR*. IEEE, July 2017.
- [4] Aviad Levis, Yoav Y Schechner, Anthony B Davis, and Jesse Loveridge. Multi-view polarimetric scattering cloud tomography and retrieval of droplet size. *Remote Sensing*, 12(17):2831, 2020.
- [5] Roi Ronen, Vadim Holodovsky, and Yoav Y. Schechner. Variable imaging projection cloud scattering tomography. *IEEE Transactions on Pattern Analysis and Machine Intelligence*, pages 1–12, 2022.
- [6] Linda Forster, Anthony B Davis, David J Diner, and Bernhard Mayer. Toward cloud tomography from space using MISR and MODIS: Locating the “veiled core” in opaque convective clouds. *Journal of the Atmospheric Sciences*, 78(1):155–166, 2021.
- [7] Aviad Levis, Yoav Y Schechner, and Ronen Talmon. Statistical tomography of microscopic life. In *Proceedings of the IEEE Conference on Computer Vision and Pattern Recognition*, pages 6411–6420, 2018.
- [8] Aviad Levis, Pratul P Srinivasan, Andrew A Chael, Ren Ng, and Katherine L Bouman. Gravitationally lensed black hole emission tomography. In *Proceedings of the IEEE/CVF Conference on Computer Vision and Pattern Recognition*, pages 19841–19850, 2022.
- [9] Sarah Brüning, Stefan Niebler, and Holger Tost. Artificial intelligence (AI)-derived 3D cloud tomography from geostationary 2D satellite data. *Atmospheric Measurement Techniques*, 17(3):961–978, 2024.
- [10] Jacob Lin, Miguel Farinha, Edward Gryspeerdt, and Ronald Clark. Volumetric cloud field reconstruction. *arXiv preprint arXiv:2311.17657*, 2023.

- [11] Xiaodong Gu, Zhiwen Fan, Siyu Zhu, Zuozhuo Dai, Feitong Tan, and Ping Tan. Cascade cost volume for high-resolution multi-view stereo and stereo matching. In *Proceedings of the IEEE/CVF conference on computer vision and pattern recognition*, pages 2495–2504, 2020.
- [12] Hamid Laga, Laurent Valentin Jospin, Farid Boussaid, and Mohammed Bennamoun. A survey on deep learning techniques for stereo-based depth estimation. *IEEE Transactions on Pattern Analysis and Machine Intelligence*, 44(4):1738–1764, 2020.
- [13] Jin Liu, Jian Gao, Shunping Ji, Chang Zeng, Shaoyi Zhang, and JianYa Gong. Deep learning based multi-view stereo matching and 3d scene reconstruction from oblique aerial images. *ISPRS Journal of Photogrammetry and Remote Sensing*, 204:42–60, 2023.
- [14] Lingdong Kong, Shaoyuan Xie, Hanjiang Hu, Lai Xing Ng, Benoit Cottreau, and Wei Tsang Ooi. Robodepth: Robust out-of-distribution depth estimation under corruptions. *Advances in Neural Information Processing Systems*, 36, 2024.
- [15] Oleg Voynov, Gleb Bobrovskikh, Pavel Karpyshov, Saveliy Galochkin, Andrei-Timotei Ardelean, et al. Multi-sensor large-scale dataset for multi-view 3d reconstruction. In *Proceedings of the IEEE/CVF Conference on Computer Vision and Pattern Recognition*, pages 21392–21403, 2023.
- [16] M. Fuentes Reyes, P. d’Angelo, and F. Fraundorfer. An evaluation of stereo and multiview algorithms for 3d reconstruction with synthetic data. *The International Archives of the Photogrammetry, Remote Sensing and Spatial Information Sciences*, XLVIII-1/W2-2023:1021–1028, 2023.
- [17] Willem Herman Steyn. Stability, pointing, and orientation. *Handbook of Small Satellites: Technology, Design, Manufacture, Applications, Economics and Regulation*, pages 145–187, 2020.
- [18] Richard Hartley and Andrew Zisserman. *Multiple View Geometry in Computer Vision*. Cambridge University Press, 2003.
- [19] Kai Zhang, Noah Snavely, and Jin Sun. Leveraging vision reconstruction pipelines for satellite imagery. In *Proceedings of the IEEE/CVF International Conference on Computer Vision Workshops*, pages 0–0, 2019.
- [20] V Jovanovic, M Smyth, and J Zong. Level 1 in-flight geometric calibration algorithm theoretical basis. *Jet Propulsion Laboratory, California Institute of Technology*, 1999.
- [21] Sameer Agarwal, Yasutaka Furukawa, Noah Snavely, Ian Simon, Brian Curless, Steven M Seitz, and Richard Szeliski. Building Rome in a day. *Communications of the ACM*, 54(10):105–112, 2011.
- [22] Jeffrey Delmerico and Davide Scaramuzza. A benchmark comparison of monocular visual-inertial odometry algorithms for flying robots. In *2018 IEEE international conference on robotics and automation*, pages 2502–2509. IEEE, 2018.
- [23] Mitch Bryson and Salah Sukkarieh. Observability analysis and active control for airborne slam. *IEEE Transactions on Aerospace and Electronic Systems*, 44(1):261–280, 2008.
- [24] Alvaro Gómez, Gregory Randall, Gabriele Facciolo, and Rafael Grompone von Gioi. An experimental comparison of multi-view stereo approaches on satellite images. In *Proceedings of the IEEE/CVF Winter Conference on Applications of Computer Vision*, pages 844–853, 2022.
- [25] Jiaxiang Hu, Anshuman Razdan, and Joseph A Zehnder. Geometric calibration of digital cameras for 3d cumulus cloud measurements. *Journal of Atmospheric and Oceanic Technology*, 26(2):200–214, 2009.
- [26] Hainan Cui, Shuhan Shen, Wei Gao, and Zhanyi Hu. Efficient large-scale structure from motion by fusing auxiliary imaging information. *IEEE Transactions on Image Processing*, 24(11):3561–3573, 2015.
- [27] Klaus Schilling, Yoav Y Schechner, and Ilan Koren. Cloudct-computed tomography of clouds by a small satellite formation. In *Proceedings of the 12th IAA symposium on Small Satellites for Earth Observation*, volume 6, page 7, 2019.
- [28] Changrak Choi and Anthony B Davis. Geoscan: Global earth observation using swarm of coordinated autonomous nanosats. In *2022 IEEE Aerospace Conference (AERO)*, pages 1–10. IEEE, 2022.
- [29] Alexander Kleinschrodt, Ilham Mammadova, Eric Jägera, Johannes Daunera, Julian Scharnagla, and Klaus Schillinga. TOM/TIM realization-a satellite earth observation (EO) formation flying mission of three nano satellites for retrieving multi view stereoscopic data. 2022.
- [30] Johannes Dauner, Lisa Elsner, Oliver Ruf, Dorit Borrman, Julian Scharnagl, and Klaus Schilling. Visual servoing for coordinated precise attitude control in the TOM small satellite formation. *Acta Astronautica*, 202:760–771, 2023.
- [31] Klaus Schilling. Small satellite formations: Challenges in navigation and its application potential. In *ICINS*, pages 1–4. IEEE, 2021.

[32] J Scharnagl, Florian Kempf, Slavi Dombrovski, and K Schilling. NetSat–challenges of a formation composed of 4 nano-satellites. In *Proceedings of the 72nd International Astronautical Congress*, 2021.

[33] David J Diner, Jewel C Beckert, Terrence H Reilly, Carol J Bruegge, James Conel, et al. Multi-angle Imaging SpectroRadiometer (MISR) instrument description and experiment overview. *IEEE Transactions on Geoscience and Remote Sensing*, 36(4):1072–1087, 1998.

[34] Iliana Genkova, Gabriela Seiz, Paquita Zuidema, Guangyu Zhao, and Larry Di Girolamo. Cloud top height comparisons from ASTER, MISR, and MODIS for trade wind cumuli. *Remote Sensing of Environment*, 107(1–2):211–222, 2007.

[35] François Marie Bréon and Marie Doutriaux-Boucher. A comparison of cloud droplet radii measured from space. *IEEE Transactions on Geoscience and Remote Sensing*, 43(8):1796–1805, 2005.

[36] Steven Platnick, Kerry G Meyer, Michael D King, Galina Wind, Nandana Amarasinghe, et al. The modis cloud optical and microphysical products: Collection 6 updates and examples from terra and aqua. *IEEE Transactions on Geoscience and Remote Sensing*, 55(1):502–525, 2016.

[37] Frédéric Parol, Jean Claude Buriez, Claudine Vanbause, Jérôme Riédi, M Doutriaux-Boucher, M Vesperini, G Sèze, P Couvert, M Viollier, FM Bréon, et al. Review of capabilities of multi-angle and polarization cloud measurements from POLDER. *Advances in Space Research*, 33(7):1080–1088, 2004.

[38] Zhengqiang Li, Weizhen Hou, Jin Hong, Fengxun Zheng, Donggen Luo, Jun Wang, Xingfa Gu, and Yanli Qiao. Directional polarimetric camera (DPC): Monitoring aerosol spectral optical properties over land from satellite observation. *Journal of Quantitative Spectroscopy and Radiative Transfer*, 218:21–37, 2018.

[39] Richard Szeliski. *Computer Vision: Algorithms and Applications*. Springer Nature, 2022.

[40] Masada Tzabari, Vadim Holodovsky, Omer Shubi, Eshkol Eytan, Ilan Koren, and Yoav Y. Schechner. Settings for spaceborne 3-D scattering tomography of liquid-phase clouds by the CloudCT mission. *IEEE Transactions on Geoscience and Remote Sensing*, 60:1–16, 2022.

[41] John Kessenich, Graham Sellers, and Dave Shreiner. *OpenGL Programming Guide: The official guide to learning OpenGL, version 4.5 with SPIR-V*. Addison-Wesley Professional, 2016.

[42] José Luis Blanco-Claraco. A tutorial on $\mathbf{se}(3)$ transformation parameterizations and on-manifold optimization. *arXiv preprint arXiv:2103.15980*, 2021.

[43] CloudCT - spaceborne cloud tomography. <https://www.cloudct.space/>.

[44] Paolo Dandini, Céline Cornet, Renaud Binet, Laetitia Fenouil, Vadim Holodovsky, Yoav Schechner, Didier Ricard, and Daniel Rosenfeld. 3D cloud envelope and cloud development velocity from simulated CLOUD/C3IEL stereo images. *Atmospheric Measurement Techniques (AMT)*, pages 1–37, 2022.

[45] Gabriela Seiz and Roger Davies. Reconstruction of cloud geometry from multi-view satellite images. *Remote Sensing of Environment*, 100(2):143–149, 2006.

[46] Jörg Gumbel, Linda Megner, Ole Martin Christensen, Nickolay Ivchenko, Donal P Murtagh, Seunghyuk Chang, Joachim Dillner, Terese Ekebrand, Gabriel Giono, Arvid Hammar, et al. The mats satellite mission–gravity wave studies by mesospheric airglow/aerosol tomography and spectroscopy. *Atmospheric Chemistry and Physics*, 20(1):431–455, 2020.

[47] Woojin Park, Arvid Hammar, Soojong Pak, Seunghyuk Chang, Jörg Gumbel, Linda Megner, Ole Martin Christensen, Jordan Rouse, and Dae Wook Kim. Flight model characterization of the wide-field off-axis telescope for the mats satellite. *Applied Optics*, 59(17):5335–5342, 2020.

[48] J UngermaNN, J Blank, J Lotz, K Leppkes, Lars Hoffmann, T Guggenmoser, M Kaufmann, P Preusse, U Naumann, and M Riese. A 3-d tomographic retrieval approach with advection compensation for the air-borne limb-imager gloria. *Atmospheric Measurement Techniques*, 4(11):2509–2529, 2011.

[49] J UngermaNN, P Preusse, E Kretschmer, and M Riese. Limited angle tomography of mesoscale gravity waves by the infrared limb-sounder gloria. *Atmos. Meas. Tech.*, 11:4327–4344, 2018.

[50] Nathaniel J Livesey, W Van Snyder, William G Read, and Paul A Wagner. Retrieval algorithms for the eos microwave limb sounder (mls). *IEEE Transactions on Geoscience and Remote Sensing*, 44(5):1144–1155, 2006.

[51] Dong L Wu, Jonathan H Jiang, and Cory P Davis. Eos mls cloud ice measurements and cloudy-sky radiative transfer model. *IEEE Transactions on Geoscience and Remote Sensing*, 44(5):1156–1165, 2006.

[52] Sean Gillies et al. Shapely: manipulation and analysis of geometric objects, 2007–.

[53] Thomas Johnson, Michel Tsamados, Jan-Peter Muller, and Julianne Stroeve. Mapping Arctic Sea-Ice Surface Roughness with Multi-Angle Imaging Spectroradiometer. *Remote Sensing*, 14(24):6249, 2022.

- [54] Roi Ronen, Yoav Y Schechner, and Eshkol Eytan. 4D cloud scattering tomography. In *Proceedings of the IEEE/CVF International Conference on Computer Vision*, pages 5520–5529, 2021.
- [55] Maximilian von Arnim, Ilham Mammadov, Lukas Draschka, Julian Scharnagl, and Klaus Schilling. The cloudct formation of 10 nano-satellites for computed tomography to improve climate predictions. In *Proceedings of the 73th International Astronautical Congress*, 2022.